HHS Public Access

Author manuscript

Bone. Author manuscript; available in PMC 2015 May 21.

Published in final edited form as:

Bone. 2014 March ; 60: 148–161. doi:10.1016/j.bone.2013.11.020.

Deletion of *Mecom* in mouse results in early-onset spinal deformity and osteopenia

Subhash C. Juneja[1,2,6], **Alin Vonica**[1], **Caroline Zeiss**[4], **Kimberly Lezon-Geyda**[3], **Bogdan Yatsula**[3], **David R. Sell**[4], **Vincent M. Monnier**[4], **Sharon Lin**[3], **Thomas Ardito**[3], **David Eyre**[5], **David Reynolds**[2], **Zhenqiang Yao**[1], **Hani A. Awad**[2,6], **Hongbo Yu**[1], **Michael Wilson**[1], **Sylvie Honnons**[1], **Brendan F. Boyce**[1], **Lianping Xing**[1,*], **Yi Zhang**[1,*], and **Archibald S. Perkins**[1,*]

[1]Department of Pathology and Laboratory Medicine, University of Rochester Medical Center

[2]Department of Orthopedics, University of Rochester Medical Center

[3]Department of Pathology, Yale University, Seattle

[4]Case Western Reserve University, Seattle

[5]University of Washington, Seattle

[6]Department of Biomedical Engineering, University of Rochester Medical Center

Abstract

Recent studies have indicated a role for a *MECOM* allele in susceptibility to osteoporotic fractures in humans. We have generated a mutation in *Mecom* in mouse (termed ME^{m1}) via *lacZ* knock-in into the upstream transcription start site for the gene, resulting in disruption of *Mds1* and *Mds1-Evi1* transcripts, but not of *Evi1* transcripts. We demonstrate that $ME^{m1/m1}$ mice have severe kyphoscoliosis that is reminiscent of human congenital or primary kyphoscoliosis. $ME^{m1/m1}$ mice appear normal at birth, but by 2 weeks, they exhibit a slight lumbar lordosis and narrowed intervertebral space. This progresses to severe lordosis with disc collapse and synostosis, together with kyphoscoliosis. Bone formation and strength testing show that $ME^{m1/m1}$ mice have normal bone formation and composition but are osteopenic. While endochondral bone development is normal, it is markedly dysplastic in its organization. Electron micrographs of the 1week postnatal intervertebral discs reveals marked disarray of collagen fibers, consistent with an inherent weakness in the non-osseous connective tissue associated with the spine. These findings indicate that lack of ME leads to a complex defect in both osseous and non-osseous musculoskeletal tissues, including a marked vertebral osteopenia, degeneration of the IVD, and disarray of

*Corresponding authors: Archibald S. Perkins, Yi Zhang, Lianping Xing and S. Juneja, archibald_perkins@urmc.rochester.edu, yi_zhang@urmc.rochester.edu, Department of Pathology and Laboratory Medicine, University of Rochester Medical Center, 601 Elmwood Ave, Rochester, NY 14642.

Conflict of Interest No authors have conflicts of interest.

connective tissues, which is likely due to an inherent inability to establish and/or maintain components of these tissues.

Graphical abstract

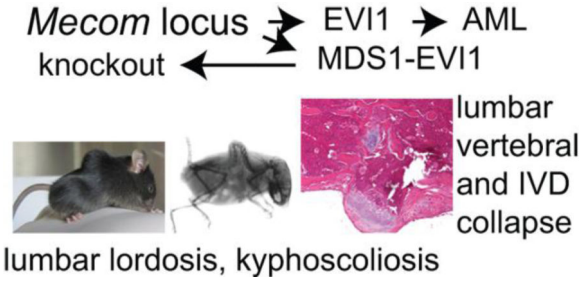

Keywords

MDS1-EVI1; congenital kyphoscoliosis; osteoporosis

INTRODUCTION

Kyphosis, including lordosis and scoliosis, is a common orthopedic problem, which can lead to destructive changes of intervertebral disc (IVD), spine deformation, back pain, decreased physical function and other clinical consequences (1–3). Kyphosis can be classified into primary and secondary types, with the latter typically being a result of the natural aging process (4, 5). Primary kyphosis, also called Scheuermann's disease, is a condition that occurs in children. This entity, which affects ~1% of the population (6), is characterized by severe spinal deformity that may lead to pain and spinal cord injury. Patients with Scheuermann's disease also have high incidence of osteoporosis (7). Though its cause is unknown, an autosomal dominant mode of inheritance has been described in some families (6, 8). Currently, no particular animal model is available to study this disease, and the pathogenesis of the spinal changes in these patients is unknown.

The combined *Mds1-Evi1 (ME) complex* locus (termed *Mecom*) is a large locus (>500 kb; see Zhang et al, (9)) with established roles in myeloid leukemogenesis and hematopoiesis. The locus harbors two distinct transcription start sites (TSS) located ~450 kb apart (9). Via the upstream TSS (termed *Mds1*), the locus produces MDS1 and MDS1-EVI1 (ME) transcripts and their encoded proteins; from the downstream TSS, it produces mRNA transcripts for at least three EVI1 isoforms (see Supplemental Figure 1 in (9)). ME and the three EVI1 isoforms possess C_2H_2-type zinc fingers that bind DNA in a sequence-specific manner (10, 11). Functioning as RNA transcriptional regulatory factors, EVI1 regulates the expression of several target genes, including *Dcn* (encoding decorin, a non-collagen extracellular matrix protein) and *Skil* (encoding Ski-like, a negative regulator of TGF-β (12)) (13) ; the role of ME in transcription is largely unknown. Among the gene products of *Mecom*, ME is distinct in that it has an N-terminal PR domain that has homology with the SET domain, which is known in some proteins to have histone methyltransferase activity

and to play a role in the establishment and maintenance of gene expression patterns during development (14).

Mecom has been shown to have an important in mammalian development. It has a pattern of expression suggesting an important role in organogenesis of the limbs, kidney, lung, and heart (15). Knockout of *Mecom* via *neo* gene insertion into exon 7, which is common to both ME and EVI1, results in embryonic lethality at 9.5 d postcoitum, with abnormalities in multiple organ systems (16). The homozygous null embryos are notable for generalized hypoplasia, suggesting a role for *Mecom* in cell proliferation at a point after organogenesis since the inception of organ formation occurs relatively normally. High level expression of *Mecom* in the limb bud is paralleled by severely retarded limb growth in the homozygous knockout embryos. Aside from the generalized hypoplasia, specific abnormalities are seen in spinal and cranial nerve development, and in the marginal layer of the neuroectoderm, which appears to be completely absent. Also notable is generalized pallor, and defects in the heart (hypoplasia, absence of trabeculae, and a looping defect) and vasculature (defective integrity of vasculature leading to extravasation of blood), accompanied by pericardial effusions and hemorrhage into body cavities and the amnion (16).

Mecom also has an essential role in hematopoiesis: it is expressed in HSCs (17–20), and disruption of the gene results in absence of functional hematopoietic precursors in the paraaortic splanchnopleural region of mouse embryos (19). Conditional deletion of exon 4 of Evi1 (also common to both ME and Evi1) results in a decreased frequency of HSCs and colony forming cells (CFCs), while no change in frequency of mature myeloid cells or lymphocytes. In addition, these mice demonstrated delayed recovery of HSCs and platelets following a myelosuppressive treatment with 5-FU (21). These results indicate that *Evi1* is indispensable for the maintenance of hematopoiesis. However, they do not distinguish between the role of ME and EVI1 mRNAs, since the targeted disruptions result in loss of both types of RNA transcripts.

In an effort to define the role of *ME* in development, we created a mutation at *ME* in mouse (termed $ME^{m1/m1}$; (9)). To our surprise, the most evident phenotype of $ME^{m1/m1}$ mice is earlyonset lumbar lordosis with kyphoscoliosis, revealing an unexpected role of ME in regulating the formation and/or maintenance of the spine and its support structures. The $ME^{m1/m1}$ mouse provides an instance of mutation in a regulatory protein leading to kyphoscoliosis. As such, the $ME^{m1/m1}$ mouse represents a unique genetic model of congenital kyphosis, the study of which will likely lead to the uncovering of novel regulatory pathways essential for the establishment and maintenance of the normal spine.

MATERIALS AND METHODS

$ME^{m1/m1}$ mice

$ME^{m1/m1}$ mice were generated as previously described (9). Briefly, the knock-in construct consists of a *lacZ* marker inserted into the first exon of *Mds1* with deletion of the splice donor, such that the insertion blocks production of both the *Mds1* and *Mds1-Evi1* transcripts; this construct was electroporated into TC-1 embryonic stem cells (derived from 129S6/SvEvTac). Genotyping was done by PCR analysis of DNA from tail biopsies of three week-

old offspring as described (9). The experiments described were performed on mice having a mixed 129SvEv/C57BL/6 background. Subsequently, the mice were backcrossed onto a C57BL/6 background; however, this was accompanied by a dramatic drop in the number of homozygous mice, and a increase in the severity of the lordosis/kyphosis. All colony maintenance was done in accordance with university and federal (US) guidelines.

Bone histology

The spine and long bone tissues were fixed 10% phosphate-buffered formalin for 72h and decalcified in 14% EDTA for 10 days, embedded in paraffin blocks. Sections (5 μm thick) were stained with hematoxylin and eosin.

Immunostaining

Radiography and Conventional and microcomputed tomography (μCT) radiology—X-ray analysis of mice was done using LX-60 Faxitron Specimen Radiogrpahy System (Faxitron X-Ray Corporation, Lincolnshire, IL) while the mice were anaesthetized. For μCT, individual vertebrae were fixed in 10% neutral buffered formalin and than transferred to 70% ethanol. The vertebrae thoracic (T) 10 to lumbar (L) vertebra 5 were used. Vertebrae were scanned at 10.5 μm on a VivaCT40 μCT scanner (Scanco Medical, Basserdorf, Switzerland) using an integration time of 300 ms, energy of 55 kVp, and intensity of 145 μA. A region of interest for quantitative analysis of trabecular bone was defined, extending from the proximal to the distal end of the vertebrae. For each sample, bone volume fraction (BV/TV), trabecular number (Tb.N), trabecular thickness (Tb.Th), trabecular separation (Tb.Sp), connectivity density (Conn.D), and height were measured.

Preparation of cleared skeletons—A dermestid beetle colony at the Peabody Museum at Yale University was employed to clear skeletons of soft tissue as described (22).

Biomechanical testing of bones—Long bones (femurs) from 3.5-month-old male $ME^{m1/m1}$ mice and WT littermates were tested using an Instron DynaMight 8841 servo-hydraulic materials testing machine (Instron, Norwood, MA) as previously described (23–26). Maximum compressive load at failure (N), maximum deformation at maximum force (mm), stiffness (N/mm), and energy to failure (area under the curve; N*mm) were measured from the recorded load-deformation curves using MATLAB software (The Mathworks, Natick, Massachusetts). Femurs were cleaned and hydrated before testing in three-point bending as previously described (25, 26).

In situ hybridization and immunohistochemistry—Whole-mount in situ hybridization (ISH) was performed as described previously (27). Indirect IHC for collagen 2a1 and 10a1 was performed as described on the University of Rochester Medical Center, Center for Musculoskeletal Research website (http://www.urmc.rochester.edu/musculoskeletal-research/core-services/histology/protocols.cfm). Briefly, vertebral columns were fixed in PFA o/n, decalcified for 4 days, paraffin embedded and sectioned coronally at 5 μm. Slides were baked for 30', rehydrated, treated with pepsin for antigen retrieval, incubated o/n with primary antibodies (anti-collagen type 2a1, Thermo Scientific #MS235-

P, 1:200, anti-collagen 10a1, Quartett #2031501005, 1:200) and visualized with Vectastain Elite Universal IgG kit (PK-6200).

Electron microscopy (EM)—Tissue samples were fixed for 24hrs at 4°C in 4.0 % paraformaldehyde and 2.5 % glutaraldehyde in 0.1 M sodium cacodylate (pH 7.4) followed by postfixation for 90 min at room temperature in 1.0 % osmium tetroxide in 0.1 M sodium cacodylate (pH 7.4). After the postfixation, the specimens were dehydrated in a graded series of ethanol to 100%, infiltrated and embedded in Epon/Araldite epoxy resin and polymerized for 2 days at 70C. One micron sections were cut and stained with Toluidine Blue to determine the appropriate area to thin section with a diamond knife at 70nm on a Reichert ultramicrotome and placed onto 200 mesh copper grids. The grids were stained with uranyl acetate and lead citrate. The sections were examined using a Hitachi 7650 transmission electron microscope at an accelerating voltage of 80 kV and photographed using a Gatan Erlangshen 11 megapixel digital camera.

Detection of allysine residues in skin collagen—Collagen was extracted from skin of mice as described (28). In brief, the process involved the following steps: 1) Delipidation with chloroform; 2) Salt/acid extraction of collagen; 3) Digestion with pepsin; 4) Freeze-dry; 5) Deamination of lysine by the extracellular enzyme lysyl oxidase, which yields 2-aminoadipic acid, or allysine. This can be detected in proteins by mass spectroscopy: 1) aldehyde group is reduced with sodium borohydrate to an alcohol; 2) protein is acid hydrolyzed; 3) alcohol and primary amine moieties are modified with trifluoroacetic anhydride to yield methyl esters and amides; 4) 6-hydroxynorleucine is quantitated with mass spectroscopy.

Western analysis of biglycan and decorin—Western blots were performed with antibodies for decorin and biglycan antibodies from Larry Fisher, NIH. The samples were digested for 1 h at 37°C with protease-free chondroitinase ABC (cat No.KE01502, Seikagaku Corp., Tokyo, Japan) at 0.005 U/0.025mL reaction (0.4 U/ml final concentration).

Statistical analysis—All results are given as mean ±SD. Comparisons between two groups were analyzed using two-tailed unpaired Student's t-test. One-way ANOVA and Dunnett's Post Hoc multiple comparisons were used for comparing three or more groups. *$p < 0.05$ were considered statistically significant.

RESULTS

Targeted mutation at the *ME* locus in the mouse

The *Mds1-Evi1 complex* (*Mecom*) locus spans over half a megabase on mouse chromosome 3 with two distinct transcription start sites (TSS) located over 450 kb apart (9): an upstream one termed *Mds1*, and a second, downstream one, termed *Evi1*. The *Mds1* TSS generates two classes of transcripts: *Mds1*, encoding 30 kDa proteins, and *Mds1-Evi1*, encoding the PR domain-containing ME protein. To assess the role of the *Mds1*/*Mds1-Evi1* TSS in development, we created a targeted disruption at this TSS by inserting a promoterless *lacZ* gene into the first coding exon in the mouse. The structure of this allele, designated ME^{m1}

(9), is such that it deletes the start methionine and splice donor to preclude production of both the MDS1 and ME mRNAs and proteins but not that of *Evi1* (9). Founders were crossed to C57BL/6 mice, and heterozygous offspring were intercrossed to create homozygotes, which were viable. RNA analysis of adult $ME^{m1/m1}$ tissues showed that *ME* transcripts are undetectable in all tissues except for a very low level in kidney (9). As expected, levels of *Evi1* mRNAs are normal (9), as they are driven off their own distinct promoter (29).

$ME^{m1/m1}$ mice develop lumbar lordosis followed by thoracic kyphosis accompanied by spine degenerative changes

By day 10, a postnatal growth delay became apparent in $ME^{m1/m1}$ mice, which resulted in significantly smaller size at adulthood for both males and females. Growth curves (Figure 1) show that homozygous mice are significantly retarded in acquiring body weight both at early (Figure 1a) and later (Figure 1b) time points of life and their maximum weight at adulthood falls well below wildtype (WT) littermates (Figure 1b). Both male and female $ME^{m1/m1}$ mice exhibited reduced fertility. We also examined heterozygotes for growth and found that they were indistinguishable from WT (data not shown).

Whereas $ME^{m1/+}$ mice appear normal, all of the $ME^{m1/m1}$ mice develop a striking lumbar lordosis and thoracic kyphoscoliosis phenotype (Figure 2a). Additional abnormalities include a slight abduction of the hind limbs (not shown) and a dorsally-positioned tail (Figure 2a, b). The phenotype develops gradually: $ME^{m1/m1}$ mice are normal at birth, but by two weeks a slight lumbar lordosis is observable compared to their WT littermates (Figure 2c); by 3 weeks the phenotype is accompanied by thoracic kyphosis (Figure 2c). This progressively worsens as the mice age and by eight weeks, the spinal deformity is quite severe (Figure 2c). Higher magnification of 2-weeks X-ray pictures show that narrower inter-vertebral spaces, including both anterior (arrow) and posterior (arrowhead) regions (Figure 2d), occur in lumbar area at 2 weeks, which is before the appearance of kyphosis. Higher magnification at ten weeks shows loss of normal vertebral articulation and obliteration of intervertebral spaces in the homozygote mutant (Figure 2e). In addition to the kyphosis and lordosis, there is also marked scoliosis (Figure 2f).

Analysis of cleared adult skeletons revealed several additional abnormalities in the spine (Figure 3). In the lumbar area there is exostosis at the epiphysis/vertebral-disc junction (Figure 3b and d, green arrows, compare to Figure 3a and c, respectively). The articular processes of lumbar vertebrae, including the prezygapophysis (pza) are fused over their dorsolateral regions (Figure 3e). There is also widening of the intervertebral spaces at the sacrolumbar and sacrococcygeal joints (Figure 3g, white and green arrow respectively, compare to Figure 3f).

Similar to gross and radiographic findings, the histologic changes in the spine were most severe in the lumbar region, but are not apparent at birth. In newborns (day 1 post birth), no histologic differences can be discerned between WT and $ME^{m1/m1}$ mice (compare Figure 4a and c with b and d). By day 10, there is mild osteopenia in the knockout mouse, but no abnormality in the intervertebral disc (compare Figure 4e and g with f and h). At 2 weeks, there is evident degeneration of the intervertebral disc at the site of the tail kink, between

CA1 and CA2 (compare 4i with j), with exostosis at the caudal end of CA1. We also observed focal delay of endochondral ossification of lumbar vertebral growth plates in *ME*$^{m1/m1}$ mice at two weeks; instead of a clearly defined physis, large blocks of unossified cartilage containing hypertrophic chondrocytes occupied the vertebral body (Figure 4l, black arrows, compare to 4k). These abnormalities affected the caudal growth plate to a greater extent than the cranial growth plate. Lumbar intervertbral discs appeared locally compressed in mutant mice, but were qualitatively similar to wildtype (not shown). Thoracic, sacral and cervical vertebrae were comparable in mutant and wildtype animals (data not shown). At 4 weeks, more marked osteopenia is observed in lumbar vertebrae of *ME*$^{m1/m1}$ mice (Figure 4n, compare to 4m), with narrowing and fusion of some lumbar discs (Figure 4n). Histologic analysis of spine of 6 weeks old *ME*$^{m1/m1}$ show various severities of disc changes in the lumbar spine. Compared to WT lumbar spine (Figure 4o), mutant animals show a progression of disc abnormalities that range from relatively normal disc morphology (Figure 4p), narrowed intervertebral space, disappearance of the nucleus pulposus and loss of cartilage (Figure 4q), and fusion of vertebrae (Figure 4r).

Micro-computerized tomography reveals *ME*$^{m1/m1}$ mice have osteopenia in the lumbar vertebrae

To examine if changes in the spine affect bone volume of *ME*$^{m1/m1}$ mice, μCT analysis was performed in individual vertebrae from T10 to L5 of day 1, day 6, day 10, and 3-month-old mice. There is no difference between WT and *ME*$^{m1/m1}$ mice at day 1 (Supplemental Figure 1a). Phenotypic differences do become apparent in the upper lumbar vertebrae in *ME*$^{m1/m1}$ specimens at day 6 and day 10, characterized by lower bone volume/total volume ratio, lower trabecular number, higher trabecular spacing, and lower connectivity. However, technical limitations, including the small size of each vertebra, limits to the voxel resolution, and the small numbers of samples, precluded establishment of statistical significance (Supplemental Figures 1b and c).

At three months, μCT showed that while thoracic vertebrae were essentially normal in morphology and bone characteristics (not shown), the lumbar vertebrae were dysmorphic with abnormal bone. Figures 5a–d depict μCT images of L2 and L3 vertebrae of WT and *ME*$^{m1/m1}$ mice, with evident dysmorphology in the *ME*$^{m1/m1}$ mice: the neural canal is abnormally large, the bone is less dense and the neural spine is wider and shorter. In addition, the centrum is abnormally shaped; there is also evident scoliosis. Quantitation of these images (N=3/genotype) confirmed the presence of osteopenia: the vertebral trabecular bone volume was markedly diminished with a decrease in vertebral trabecular thickness, trabecular number, and connectivity density (Figure 5e). The vertebrae in *ME*$^{m1/m1}$ were also slightly smaller and shorter than WT (Figure 5, compare d to c; Figure 5e). These changes were particularly pronounced in L2 and L3. In contrast, no differences were observed in thoracic spine. Thus, the defect appears to be concentrated in the lumbar region, which parallels the observation that the lumbar lordosis temporally precedes the thoracic kyphosis, and suggests that the former leads to the latter.

No obvious abnormality in long bones of *ME$^{m1/m1}$* mice

To determine the effect of ME depletion on appendicular skeleton, we examined morphology and bone formation rate in long bone (femurs) sections of 2–3-month-old *ME$^{m1/m1}$* mice and WT littermates, as well as bone strength. No difference in bone volume, bone formation rate and mineral apposition rate was observed (data not shown). Osteoclast formation from spleen cells in osteoclastogenic assay was normal (data not shown). Consistent with these observations, serum calcium, phosphorus and osteocalcin levels were comparable between WT and *ME$^{m1/m1}$* mice (data not shown). Interestingly, bio-mechanical testing of femurs from mutant and WT male mice (3.5 months of age) revealed decrease in bone strength (Table 1, a and b). These studies suggest that the bone defects in the spine of *ME$^{m1/m1}$* mice is more predominant than that seen in the long bones.

Endochondral bone formation appears normal in *ME$^{m\ 1/m\ 1}$* mice: Analysis of vertebrae for Ihh, PTHRP-R, Collagen2 and Collagen 10

The gross and histologic morphological appearance of the vertebral column in *Mds1*−/− mice suggested a primary abnormality in the maintenance of the skeletal structure in the adult, either in the bone itself or in the intervertebral disc. The vertebrae are created through endochondral bone formation, but unlike the bones of the appendicular skeleton, have only one ossification center. There is a single epiphyseal center at each end of the bone abutting the cartilaginous joint surface, which, in the case of the vertebral body, adjoins the intervertebral disc. We considered it possible that the kyphotic phenotype was due to a problem in the maintenance of bone in the adult, since at birth the axial skeleton in homozygotes and wildtypes were indistinguishable.

Endochondral bone formation originates with progenitor cells located beneath the cartilaginous endplate, which proliferate, migrate, and differentiate into matrix-producing chondrocytes. This differentiation occurs in a stepwise manner, wherein the cells mature from prehypertrophic to hypertrophic chondrocytes, which is accompanied by a transition from mitotic to postmitotic cell type, and a dramatic increase in the production of matrix components, particularly collagen type II. This matrix then becomes calcified to produce the primary bony template that is then invaded by osteoblasts and osteoclasts, and actively remodeled to make mature trabecular and cortical bone. Key regulators of this process include Indian Hedgehog (Ihh), which is secreted by chondrocytes and stimulates the secretion of Parathyroid hormone-related protein (PTHRP), which then acts as a mitogen on the precursor cells to promote their appropriate expansion in the subarticular zone. Mutation of either PTHrP (30) or its receptor (31) result in premature maturation of chondrocytes and foreshortened, thickened bones. While PTHrP is expressed at highest levels in the periarticular perichondrium, PTH/PTHrP-R is expressed at highest levels in the mitotically active prehypertrophic chondrocytes (32). *Ihh* is expressed by the postmitotic prehypertrophic chondrocytes, and regulates the expression of PTHrP in the periarticular perichondrial cells as part of a feedback loop that delays the premature maturation of chondrocytes and assuring the proper placement of transit to the postmitotic state (33). This regulatory network is essential for proper bone development.

To examine the process of endochondral bone more closely, we performed in situ hybridization for Ihh and PTHRP, to document the presence of these key factors, but also to assess the presence and location of the cellular compartment that produces these factors. Thus, radiolabeled sense and antisense probes were prepared for *Ihh* and *Ppr*, and were hybridized to sections of vertebrae from adult wildtype and $ME^{m1/m1}$ mice. Autoradiography revealed hybridization of the *Ppr* probe in both mutant and wildtype specimens within the prehypertrophic chondrocytes as reported previously (32). Figure 6 a–d shows photomicroscopy under darkfield microscopy of wildtype and mutant sections, with the latter specimen being at a point of severe deformity, with loss of integrity of the intervertebral disc and malformation of the physis. Nonetheless, a zone of *Ppr*-expressing cells is present, albeit severely perturbed by the disruption of normal structure. Brightfield illumination shows the same pattern, and allows identification of the zones of chondrocyte maturation (Figure 6e, f). Similarly, *Ihh* expression was detected in both wildtype and mutant specimens, within the postmitotic prehypertrophic chondrocytes (Figure 6, g–l). Again, while there is clear disruption and distortion of the zone of *Ihh* expression, the expression is qualitatively in the proper location.

We also performed immunohistochemical stains for collagen type II, which is secreted by chondrocytes, including those of the intervertebral disc (34), and collagen type 10a1, present in hypertrophic chondrocytes of the growth plate during mineralization (35). No difference in expression was seen between WT and $ME^{m1/m1}$ homozygous newborn mice for either Col II (Figure 6, m, n) or Col X (Figure 6 o , p). These findings are consistent with an essentially normal developmental process for chondrocytes within mutant mice. They also suggest that a change in collagen synthesis is probably not the cause of the IVD and vertebral body defects.

Based on these studies and on examination of histologic H&E-stained sections, it is eviden that while major abnormalities exist in the structure of the vertebral column, the process of endochondral bone formation in the adult $ME^{m1/m1}$ mice occurs normally: the key cellular components of the process are present and are producing two of the major regulators in the appropriate compartment; the two major collagens that mark chondrocyte compartments are also appropriately expressed.

Abnormality of collagen fibers in intervertebral discs and tendons of $ME^{m1/m1}$ mice

We further determine if the intervertebral disc was abnormal in these mice. A powerful way of assessing this is through ultrastructural analysis, which allows assessment of collagen fibril structure. Noting the collapse of the IVD in lumbar spines of $ME^{m1/m1}$ mice, we performed ultrastructural studies on IVD of mice at one week of age. In WT mice, this revealed evenly spaced collagen fibers of fairly uniform diameter in parallel orientation, with the occasional presence of orthogonally-oriented fascicles in some fields (Figure 7a, top). In contrast, $ME^{m1/m1}$ mice displayed fibers of markedly varying diameter, with little consistency apparent in their orientation (Figure 7a, bottom).

We also examined the ultrastructure of collagen fibril of ligaments and tendons from different locations including sacrum, tail, and Achilles of $ME^{m1/m1}$ and WT mice. Photomicrographs illustrated that the average fibril diameter in all the specimens examined

was smaller in sacral ligaments and tail tendons from *ME*$^{m1/m1}$ mice (Fig 7b–c, respectively). For both locations, there were a greater number of fibrils per area in *ME*$^{m1/m1}$ mice; WT sacral ligament had 252 fibrils while *ME*$^{m1/m1}$ had 502; WT tail tendon had 90 while *ME*$^{m1/m1}$ had 224. Similar findings were observed in the Achilles tendons (avg. dia. 133+149 nm in WT vs 79+95 nm in *ME*$^{m1/m1}$; 267 count in WT vs 398 in *ME*$^{m1/m1}$). These findings are consistent with a fundamental deficiency in the ability of *ME*$^{m1/m1}$ tendon fibrils to fuse into larger-sized fibrils, or, the larger fibrils are formed but are less stable.

Assessment of connective tissue abnormalities in *ME*$^{m1/m1}$ mice

To determine if the abnormalities in mutant mice might be due to abnormal post-translational processing of collagen, collagen α1(I) and α2(I) chains from bone (and α1(II) from cartilage) were gel purified and submitted for mass spectroscopy to screen for changes in 3-hydroxyproline and lysine hydroxylation. The analyses revealed no effect on these post-translational modifications by the mutation in *ME* (data not shown). To further assess the modification of collagen, skin collagen samples were analyzed for evidence of lysyl oxidase-mediated lysine deamination, the first step in lysine modification that leads to collagen crosslinking. The product of lysine deamination is allysine, which can be quantitated by further oxidation to 2-aminoadipic acid or reduction to norleucine; crosslinked lysine residues will be resistant to these modifications. A defect in lysyl oxidase would result in lower levels of allysine, and hence lower levels of 6-OH norleucine and 2-aminoadipic acid per mol lysine. As shown in Figure 7d, the levels of 6-OH norleucine and 2-aminoadipic acid in skin collagen were no different between wildtype and *ME*$^{m1/m1}$ mice.

Abundance of DCN and BGN in bone is normal

Given the complex phenotype *of ME*$^{m1/m1}$ mice, we wished to see if there were any defects in the expression of *Dcn* and *Bgn* was also seen in bone. Instead of assaying cultured explants of bone cells, we directly assayed bone for levels of DCN and BGN proteins by Western blot, before and after chondroitinase treatment, which removes the extensive glycosylation. This analysis, performed on lumbar vertebrae of 2-week old mice, revealed no apparent difference in DCN or BGN amount or molecular weight in the lumbar vertebrae (Figure 7e).

Expression of *ME* in both bone and tendon

Phenotypic analyses of the *ME*$^{m1/m1}$ mouse provided above suggest that the underlying mechanism is very likely highly complex, with abnormalities seen both in the vertebrae (osteopenia) and in the tendons (decreased strength and diameter). One critical parameter in deciphering the mechanism is to determine where *ME* is expressed. To that end, RNA analysis was performed of vertebral bone by quantitative rt-PCR, with comparison to kidney (a known positive control (15)) and to DA-1 cells, which do not express the gene. This revealed significant expression of the *ME* gene in both kidney and in spine, but not in DA-1 cells (Figure 8a). Because tendon and ligament are derived from the same precursors (36, 37), we examined the expression levels of *ME* in mRNA extracted from tenocyte cultures and compared this with WT kidney, primary bone marrow stromal cells (BMSC) and NIH 3T3 cells (Figure 8b). As previously reported (15), *ME* was highly expressed in WT kidney.

Impressively, it also highly expressed in WT tendons; *ME* mRNA was significantly lower in bone marrow stromal cells and was not detected in 3T3 fibroblasts.

DISCUSSION

Spinal deformity in *ME*$^{m1/m1}$ mice is complex

We have generated *ME*$^{m1/m1}$ mice and found that they develop a spontaneous kyphoscoliosis that begins with lumbar lordosis and sacral instability; this is followed by thoracic kyphosis and degenerative changes in the vertebral bones. The effect of the mutation is complex, affecting multiple tissue types including bone, which is osteopenic, intervertebral disc, which shows degenerative changes and dysmorphic collagen fibrils, and spinal support structures, which have smaller collagen fibril size and decreased strength. Thus, both the spine itself and its support structures are affected. Given that *ME* encodes a DNA-binding transcription factor, our uncovering of a role for ME in the establishment and maintenance of a normal spine represents an important discovery that should allow elucidation of novel regulatory pathways critical for the spine development and homeostasis.

Degenerative discs and kyphoscoliosis with mutation of other trascription factors

We describe abnormal ossification of the endochondral bone formation in the lumbar vertebrae, associated with degeneration of the intervertebral disc within the lumbar region. Interestingly, a similar phenotype has been described in strains of mice bearing mutations in other transcription factors, including NFIX, EGR3, FRA2, KKT, PAX1, and UNC4 (see Supplemental Table 1). For instance, our phenotype is similar to that seen in a mouse knockout of the *Nfix*, which shows a delay in ossification, thoracic kyphosis, lumbar lordosis, and scoliosis (38). Other transcription factors for which mutation results in kyphosis include FRA2 (endoded by *Fosl2*) (39), a member of the Fos family of AP1-associated transcription factors, of which many play a role in bone formation. The major AP1 form in bone appears to be Fra2:cJun dimers, and deletion of c-Jun also results in altered disc development and kyphosis (40). AP1 helps regulate *Clec3b*, encoding tetranectin (41) which plays a role in tissue remodeling, and mutation of *Clec3b* leads to defects of the intervertebral disc (42). Interestingly, NFIX also regulates *Clec3b*.

Signaling pathways involving ME

To identify the downstream signaling molecules that mediate the effect of *ME* on spine, we are particularly considering TGF-β because 1) it has been reported that EVI1 physically interacts with SMAD proteins and thereby antagonizes TGF-β signaling (43, 44). ME binds to SMAD proteins as well, and can also repress TGF-β signaling, though not as effectively as EVI1 (45). 2) TGF-β plays an important role in tendon/ligament cell development (46). 3) TGF-β regulates ECM gene expression (47). 4) Deletion of TGF-β2 in the mouse results in abnormal vertebral development, with failure of the neural arch closure (48). In addition, effects of the TGF-β family member GDF-5 (also known as myostatin) are to modulate muscle growth; in KO mice lacking GDF-5, there is increased muscle mass, and, concomitantly, an increase in the size of bone at muscle attachment sites and increased bone density (49). It appears thus that changes in muscle strength can result in associated changes

in bone growth at the points of attachment. In our mice, there is decreased size of the vertebral spinous process, to which intraspinous muscles attach.

Is the *ME*$^{m1/m1}$ mouse a model for Scheuermann disease?

Spine deformities, including kyphosis, lordosis and scoliosis, are common orthopedic problems, which can lead to destructive changes of IVD, spine deformation, back pain, decreased range of motion and other clinical consequences (1–3). Primary kyphosis, or Scheuermann disease, occurs in childhood or adolescence, and is characterized by severe spinal deformity with back pain and potential spinal cord injury. The similarities between our model and Scheuermann's disease include the following: wedging of affected vertebrae, normal mineralization of bone, abnormal ossification of endochondral bone, and erosion of vertebral endplate, with invasion of the disc into the vertebral body (50). Scheuermann's is also associated with an abnormal anterior extension of affected vertebrae (50). We see something similar in our mice, in that the affected vertebrae show exostoses on the centrum at the margin between the disc and the centrum. In Scheuermann's, the onset is typically late childhood to adolescence; in mice, this likely corresponds to the period from 3–5 weeks, which is when the phenotype becomes evident. We do see changes at earlier time points; whether this is the case in Scheuermann's has not been studied. Dissimilarities include more marked severity in the lumbar spine in our model, as compared with the thoracic spine in Scheuermann's; Scheuermann disease is fairly common, affecting about 1% population (6); while its cause is unknown, it is likely heterogeneous. A study of monozygotic and dizigotic twins found a substantially higher incidence in monozygotic twins (51), indicating a genetic component. In addition, an autosomal dominant mode of inheritance has been described in some families (6, 8), while in others, nongenetic causes are speculated, including a growth abnormality of the vertebrae as result of trauma, or hormonal and nutritional etiologies. Others speculate the disease results from impaired spinal stability due to tendon/ligament weakness and/or laxity. However, these speculations have never been investigated in experimental models. Defective collagen fibers in tendon and ligament cells have reported in several genetic diseases; one in particular is EDS, in which abnormalities in collagen fibrils are observed in all six subtypes (52). One of the EDS subtypes, termed kyphoscoliotic type (or EDS type VI), exhibits spinal instability and kyphoscoliosis (53, 54). However, these patients have severe abnormality in other parts of the body, including corneal fragility and joint hypermobility, muscle hypotonia at birth, and arterial rupture (52). While *ME*$^{m1/m1}$ mice do have kyphoscoliosis, they lack hypotonia; whether or not they have corneal or skin fragility or joint laxity has not been formally addressed. While EDS has abnormalities in multiple organs, the abnormalities of Scheuermann disease occur only in the spine, with no recurring or characteristic findings in other organ systems. Whether or not *ME* is the pathogenic gene for Scheuermann disease needs to be tested with DNA samples from Scheuermann's patients.

A link between a single nucleotide polymorphism (SNP) at *MECOM* and human bone disease has recently been demonstrated by genome-wide association study by Hwang and coworkers (55). They identified human variant of *MECOM*, associated with SNP *rs784288*, as a novel predisposing factor of osteoporotic fractures (OF) in Asian women ($p=3.59\times10^{-8}$; OR 1.39). Interestingly, based on expression levels in Epstein-Barr virus-transformed

lymphoblastoid cell lines, this OF-associated allele of *MECOM* shows increased expression of of the gene relative to other alleles; however, the fold upregulation was not indicated, nor was RNA expression analysis performed directly in osteoclasts or bone cells derived from patients bearing OF-susceptible allele versus controls. Further complicating matters is that targeted resequencing of the *MECOM* gene in 164 cases of OF and 818 controls revealed additional OF-associated SNPs at *MECOM*, and perhaps these result in production of a hypofunctional ME protein (55). While the findings of Hwang et al clearly show an association between one specific *MECOM* allele in human populations and risk of OF, the mechanism by which this allele predisposes to fractures is not clear. Our ME mouse model thus provides a valuable tool to further dissect this human disease and its molecular mechanisms for therapeutic intervention in future.

Supplementary Material

Refer to Web version on PubMed Central for supplementary material.

ACKNOWLEDGMENTS

The authors would like to thank Drs. Marvin Tanzer, Michael Kashgarian, Roland Baron, William Horne, Mark Horowitz, Caren Gundberg, Randy Rosier, Regis O'Keefe, William Philbrick, and Di Chen for valuable discussion; George Steele-Perkins, Mary Ann Weiss, Karen Bentley, Yanyun Li, Gregory J. Watkns-Cowell, Diana Sanchez, Nathaniel Miller, JP Zhang, and Chris Razivi, for technical assistance; Marian Young for anti-decorin and anti-biglycan antibodies. We also acknowledge the Molecular Core of the Yale Core Center for Musculoskeletal Disorders (NIH AR46032), and the University of Rochester Core Center for Musculoskeletal Biology and Medicine (URCCMBM) Public Health Service Award from NIAMS to Ed Schwarz/Yi Zhang P30AR061307. Hongbo Yu is supported by a fellowship from Department of Oral and Craniomaxillofacial Science, Ninth People's Hospital, Shanghai Jiao Tong University School of Medicine, Shanghai, China, 200011.

This work was funded by NIH R01 CA112188 to ASP; AR48696 to XLP; Public Health Servic Award from NIAMS, P30AR061307 to Ed Schwarz/YZ and AR56696 to HA; HY is supported by a training fellowship from Ninth People's Hospital, Shanghai Jiao Tong University School of Medicine.

Literature Cited

1. Sinaki M, Brey RH, Hughes CA, Larson DR, Kaufman KR. Balance disorder and increased risk of falls in osteoporosis and kyphosis: significance of kyphotic posture and muscle strength. Osteoporos Int. 2005 Aug; 16(8):1004–1010. PubMed PMID: 15549266. [PubMed: 15549266]
2. Kado DM, Duong T, Stone KL, Ensrud KE, Nevitt MC, Greendale GA, et al. Incident vertebral fractures and mortality in older women: a prospective study. Osteoporos Int. 2003 Jul; 14(7):589–594. PubMed PMID: 12827222. [PubMed: 12827222]
3. Roux C, Fechtenbaum J, Kolta S, Said-Nahal R, Briot K, Benhamou CL. Prospective Assessment of Thoracic Kyphosis in Postmenopausal Women With Osteoporosis. J Bone Miner Res. 2009 Jul 13. PubMed PMID: 19594302.
4. Schneider DL, von Muhlen D, Barrett-Connor E, Sartoris DJ. Kyphosis does not equal vertebral fractures: the Rancho Bernardo study. J Rheumatol. 2004 Apr; 31(4):747–752. PubMed PMID: 15088302. [PubMed: 15088302]
5. Bartynski WS, Heller MT, Grahovac SZ, Rothfus WE, Kurs-Lasky M. Severe thoracic kyphosis in the older patient in the absence of vertebral fracture: association of extreme curve with age. AJNR Am J Neuroradiol. 2005 Sep; 26(8):2077–2085. PubMed PMID: 16155162. [PubMed: 16155162]
6. Findlay A, Conner AN, Connor JM. Dominant inheritance of Scheuermann's juvenile kyphosis. J Med Genet. 1989 Jun; 26(6):400–403. PubMed PMID: 2738903. [PubMed: 2738903]
7. Lopez R, Burke S, Levine D, Schneider R. Osteoporosis in Scheuermann's disease. Spine. 1988; 13(10):1099–1103. [PubMed: 3206267]

8. Garoflid N, Fragniere B, Dutoit M. ["Round back" in children and adolescents]. Rev Med Suisse Romande. 2000 Oct; 120(10):815–820. PubMed PMID: 11109912. Le "dos rond" de l'enfant et de l'adolescent. [PubMed: 11109912]
9. Zhang Y, Stehling-Sun S, Lezon-Geyda K, Juneja S, Coillard L, del Campo J, et al. Mds1-Evi1 is critical for long-term hematopoietic stem cells function by regulating p57-Kip2. Blood. 2011; 118:3853–3861. [PubMed: 21666053]
10. Perkins AS, Fishel R, Jenkins NA, Copeland NG. Evi-1, a murine zinc finger proto-oncogene, encodes a sequence-specific DNA-binding protein. Mol Cell Biol. 1991 May; 11(5):2665–2674. PubMed PMID: 2017172. [PubMed: 2017172]
11. Funabiki T, Kreider BL, Ihle JN. The carboxyl domain of zinc fingers of the Evi-1 myeloid transforming gene binds a consensus sequence GAAGATGAG. Oncogene. 1994; 9:1575–1581. [PubMed: 8183551]
12. Stroschein S, Wang W, Zhou S, Zhou Q, Luo K. Negative Feedback Regulation of TGF-β Signaling by the SnoN Oncoprotein. Science. 1999; 286:771–774. [PubMed: 10531062]
13. Yatsula B, Lin S, Read A, Poholek A, Yates K, Yue D, et al. Identification of binding sites of EVI1 in mammalian cells. J Biol Chem. 2005; 280:30712–30722. [PubMed: 16006653]
14. Schwartz Y, Pirrotta V. Polycomb complexes and epigenetic states. [Review]. Curr Opin Cell Biol. 2008; 20:266–273. [PubMed: 18439810]
15. Perkins AS, Mercer JA, Jenkins NA, Copeland NG. Patterns of Evi-1 expression in embryonic and adult tissues suggest that Evi-1 plays an important role in mouse development. Development. 1991; 111:479–487. [PubMed: 1893871]
16. Hoyt PR, Bartholomew C, Davis AJ, Yutzey K, Gamer LW, Potter SS, et al. The Evi1 proto-oncogene is required at midgestation for neural, heart, and paraxial mesenchyme development. Mech Dev. 1997 Jul; 65(1–2):55–70. PubMed PMID: 9256345. [PubMed: 9256345]
17. Phillips R, Ernst R, Brunk B, Ivanova N, Mahan M, Deanehan J, et al. The genetic program of hematopoietic stem cells. Science. 2000; 288(5471):1635–1637. [PubMed: 10834841]
18. Shimizu S, Nagasawa T, Katoh O, Komatsu N, Yokota J, Morishita K. EVI1 is expressed in megakaryocyte cell lineage and enforced expression of EVI1 in UT-7/GM cells induces megakaryocytic differentiation. Biochem Biophys Res Comm. 2002; 292(3):609–616. [PubMed: 11922610]
19. Yuasa H, Oike Y, Iwama A, Nishikata I, Sugiyama D, Perkins A, et al. Oncogenic transcription factor Evi1 regulates hematopoietic stem cell proliferation through GATA-2 expression. Embo J. 2005; 24(11):1976–1987. [PubMed: 15889140]
20. Park I-K, He Y, Lin F, Laerum O, Tian Q, Bumgarner R, et al. Differential gene expression profiling of adult murine hematopoietic stem cells. Blood. 2002; 99(2):488–498. [PubMed: 11781229]
21. Goyama S, Yamamoto G, Shimabe M, Sato T, Ichikawa M, Ogawa S, et al. Evi-1 is a critical regulator for hematopoietic stem cells and transformed leukemic cells. Cell Stem Cell. 2008 Aug 7; 3(2):207–220. PubMed PMID: 18682242. [PubMed: 18682242]
22. Hefti E, Trechsel U, Rüfenacht H, Fleisch H. Use of dermestid beetles for cleaning bones. Calcif Tissue Int. 1980; 31:45–47. [PubMed: 6770972]
23. Hasslund S, Jacobson JA, Dadali T, Basile P, Ulrich-Vinther M, Soballe K, et al. Adhesions in a murine flexor tendon graft model: autograft versus allograft reconstruction. J Orthop Res. 2008 Jun; 26(6):824–833. PubMed PMID: 18186128. [PubMed: 18186128]
24. Guo R, Yamashita M, Zhang Q, Zhou Q, Chen D, Reynolds DG, et al. Ubiquitin Ligase Smurf1 Mediates Tumor Necrosis Factor-induced Systemic Bone Loss by Promoting Proteasomal Degradation of Bone Morphogenetic Signaling Proteins. J Biol Chem. 2008 Aug 22; 283(34): 23084–23092. PubMed PMID: 18567580. [PubMed: 18567580]
25. Xiao Z, Awad H, Liu S, Mahlios J, Zhang S, Guilak F, et al. Selective Runx2-II deficiency leads to low-turnover osteopenia in adult mice. Dev Biol. 2005; 283:345–356. [PubMed: 15936013]
26. Liu S, Brown T, Zhou J, Xiao Z, Awad H, Guilak F, et al. Role of matrix extracellular phosphoglycoprotein in the pathogenesis of X-linked hypophosphatemia. J Am Soc Nephrol. 2005; 16(6):1645–1653. [PubMed: 15843468]

27. Wilkinson, DG. Whole-mount in situ hybridisation of vertebrate embryos. In: Wilkinson, DG., editor. In Situ Hybridisation: A Practical Approach. Oxford: IRL Press; 1992. p. 75-83.
28. Sell D, Strauch C, Shen W, Monnier V. 2-aminoadipic acid is a marker of protein carbonyl oxidation in the aging human skin: effects of diabetes, renal failure and sepsis. Biochem J. 2007; 404:269–277. [PubMed: 17313367]
29. Bartholomew C, Morishita K, Askew D, Buchberg D, Jenkins NA, Copeland NG, et al. Retroviral insertions in the *CB-1*/ *Fim-3* common site of integration active expression of the *Evi*-1 gene. Oncogene. 1989; 4:529–534. [PubMed: 2542863]
30. Karaplis A, Luz A, Glowacki J, Bronson R, Tybulewicz V, Kronenberg H, et al. Lethal skeletal dysplasia from targeted disruption of the parathyroid hormone-related peptide gene. Genes & Dev. 1994; 8:277–289. [PubMed: 8314082]
31. Lanske B, Karaplis A, Lee K, Luz A, Vortkamp A, Pirro A, et al. PTH/PTHrP receptor in early development and Indian hedgehog-regulated bone growth. Science. 1996; 273:663–666. [PubMed: 8662561]
32. Lee K, Deeds J, Segre G. Expression of parathyroid hormone-related peptide and its receptor messenger ribonucleic acids during fetal development of rats. Endocrinology. 1995; 136:453–463. [PubMed: 7835276]
33. Chung U, Schipani E, McMahon A, Kronenberg H. Indian hedgehog couples chondrogenesis to osteogenesis endochondral bone development. J Clin Invest. 2001; 107:295–304. [PubMed: 11160153]
34. Yang C, Rui H, Mosler S, Notbohm H, Sawaryn A, Müller P. Collagen IIfrom articular cartilage and annulus fibrosus Structural and functional implication of tissue specific posttranslational modifications of collagen molecules. Eur J Biochem. 1993; 213(3):1297–1302. [PubMed: 8504821]
35. Boos N, Nerlich A, Wiest I, von der Mark K, Aebi M. Immunolocalization of type X collagen in human lumbar intervertebral discs during ageing and degeneration. Histochem Cell Biol. 1997; 108(6):471–480. [PubMed: 9450629]
36. Murchison ND, Price BA, Conner DA, Keene DR, Olson EN, Tabin CJ, et al. Regulation of tendon differentiation by scleraxis distinguishes force-transmitting tendons from muscle-anchoring tendons. Development. 2007 Jul; 134(14):2697–2708. PubMed PMID: 17567668. [PubMed: 17567668]
37. Pryce BA, Watson SS, Murchison ND, Staverosky JA, Dunker N, Schweitzer R. Recruitment and maintenance of tendon progenitors by TGFbeta signaling are essential for tendon formation. Development. 2009 Apr; 136(8):1351–1361. PubMed PMID: 19304887. [PubMed: 19304887]
38. Driller K, Pagenstecher A, Uhl M, Omran H, Berlis A, Grunder A, et al. Nuclear factor I X deficiency causes brain malformation and severe skeletal defects. Mol Cell Biol. 2007 May 15; 27(10):3855–3867. [PubMed: 17353270]
39. Karreth F, Hoebertz A, HScheuch H, Eferl R, Wagner E. The AP1 transcription factor Fra2 is required for efficient cartilage development. Development. 2004; 131:5717–5725. [PubMed: 15509771]
40. Behrens A, Haigh J, Mechta-Grigoriou F, Nagy A, Yaniv M, Wagner E. Impaired intervertebral disc formation in th absence of *Jim* . Development. 2003; 130:103–109. [PubMed: 12441295]
41. Sorensen CB, Berglund L, Petersen TE. Cloning of the murine tetranectin gene and 5'-flanking region. Gene. 1997; 201(1–2):199–202. [PubMed: 9409787]
42. Iba K, Durkin M, Johnsen L, Hunziker E, Damgaard-Pedersen K, Zhang H, et al. Mice with a targeted deletion of the tetranectin gene exhibit a spinal deformity. Mol Cell Biol. 2001; 21:7817–7825. [PubMed: 11604516]
43. Alliston T, Ko T, Cao Y, Liang Y-Y, Feng X-H, Chang C, et al. Repression of bone morphogenetic protein and activin-inducible transcription by Evi-1. J Biol Chem. 2005; 280:24227–24237. [PubMed: 15849193]
44. Kurokawa M, Mitani K, Imai Y, Ogawa S, Yazaki Y, Hirai H. The t(3;21) fusion product, AML1/ Evi-1, interacts with Smad3 and blocks transforming growth factor-beta-mediated growth inhibition of myeloid cells. Blood. 1998 Dec 1; 92(11):4003–4012. PubMed PMID: 9834202. [PubMed: 9834202]

45. Nitta E, Izutsu K, Yamaguchi Y, Imai Y, Ogawa S, Chiba S, et al. Oligomerization of Evi-1 regulated by the PR domain contributes to recruitment of corepressor CtBP. Oncogene. 2005; 24:6165–6173. [PubMed: 15897867]

46. Lorda-Diez CI, Montero JA, Martinez-Cue C, Garcia-Porrero JA, Hurle JM. Transforming Growth Factors Œ≤ Coordinate Cartilage and Tendon Differentiation in the Developing Limb Mesenchyme. Journal of Biological Chemistry. 2009 Oct 23; 284(43):29988–29996. [PubMed: 19717568]

47. Roberts A, Heine U, Flanders K, Sporn M. TGF-β: Major role in regulation of extracellular matrix. Ann NY Acad Sci. 1990; 580:225–232. [PubMed: 2186691]

48. Sanford LP, Ormsby I, Gittenberger-de Groot AC, Sariola H, Friedman R, Boivin GP, et al. TGFbeta2 knockout mice have multiple developmental defects that are non-overlapping with other TGFbeta knockout phenotypes. Development. 1997 Jul 1; 124(13):2659–2670. [PubMed: 9217007]

49. Hamrick MW, Pennington C, Byron CD. Bone architecture and disc degeneration in the lumbar spine of mice lacking GDF-8 (myostatin). Journal of Orthopaedic Research. 2003; 21(6):1025–1032. [PubMed: 14554215]

50. Scoles P, Latimer B, Digiovanni B, Vargo E, Bauza S, Jellema L. Vertebral alterations in Scheuermann's kyphosis. Spine. 1991; 16(5):509–515. [PubMed: 2052992]

51. Damborg F, Engell V, Andersen M, Kyvik K, Thomsen K. Prevalence, concordance, and heritability of Scheuermann kyphosis based on a study of twins. The Journal of Bone and Joint Surgery. 2006; 88A(10):2133–216. [PubMed: 17015588]

52. Beighton P, De Paepe A, Steinmann B, Tsipouras P, Wenstrup R. Ehlers-Danlos Syndromes: Revised Nosology, Villefranche, 1997. Am J Med Genet. 1998; 77:31–37. [PubMed: 9557891]

53. Gasik R, Styczynski T. Atypical symptom of Ehlers-Danlos syndrome impeding diagnosis: feeling of spinal instability. J Rheumatol. 2009 Aug; 36(8):1847–1848. PubMed PMID: 19671830. [PubMed: 19671830]

54. Grahame R. Joint hypermobility syndrome pain. Curr Pain Headache Rep. 2009 Dec; 13(6):427–433. PubMed PMID: 19889283. [PubMed: 19889283]

55. Hwang J, Lee S, Go M, Kim B, Kou I, Ikegawa S, et al. Meta-analysis identifies a MECOM gene as a novel predisposing factor of osteoporotic fracture. J Med Genet. 2013

Highlights

- Mouse model for congenital kyphoscoliosis caused by a mutation in transcriptional regulator *Mds1-Evi1*.
- Lumbar lordosis and sacral instability precede thoracic kyphosis.
- Bone is osteopenic within the lumbar area.
- Findings suggest an underlying abnormality also occurs in spinal support structures, leading to spinal degenerative changes.

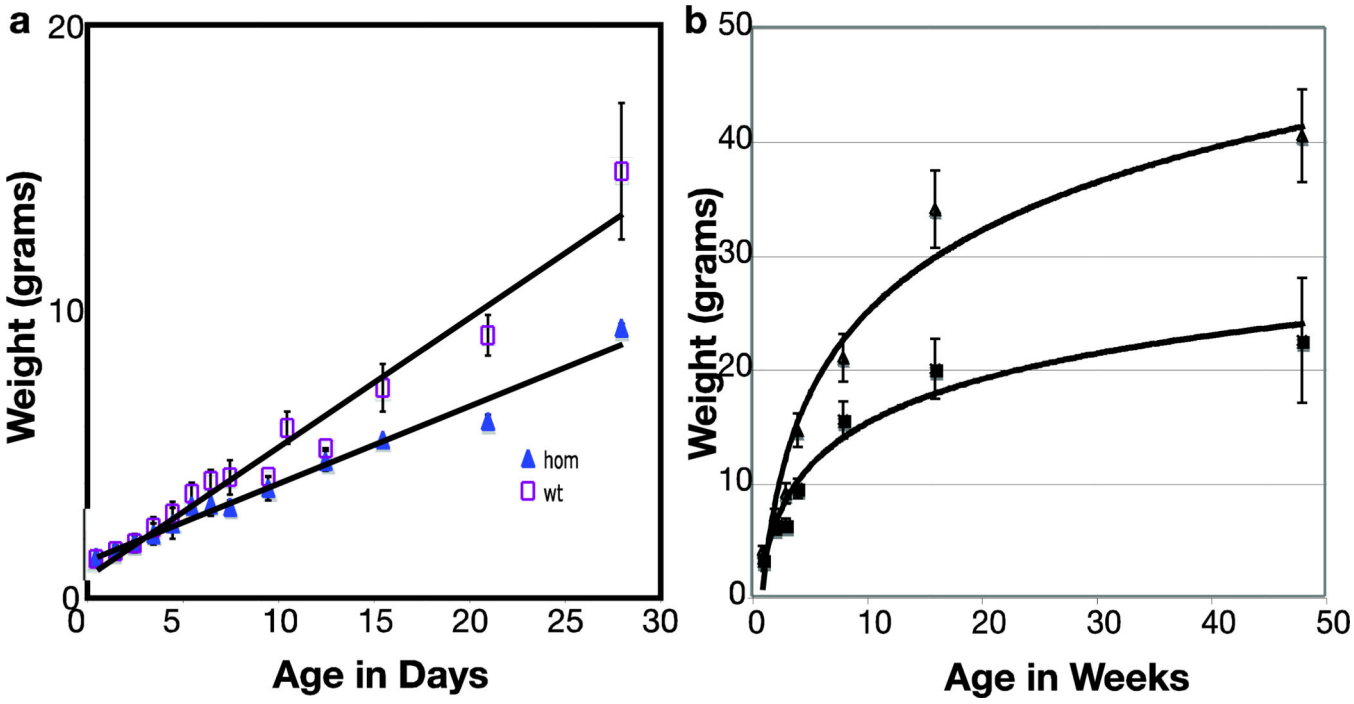

Figure 1.

Growth curves for *ME*$^{m1/m1}$ (n=7) and WT (n=20) mice, an equal mix of both genders. a) early phase of growth; b) all time points; $p<0.01$.

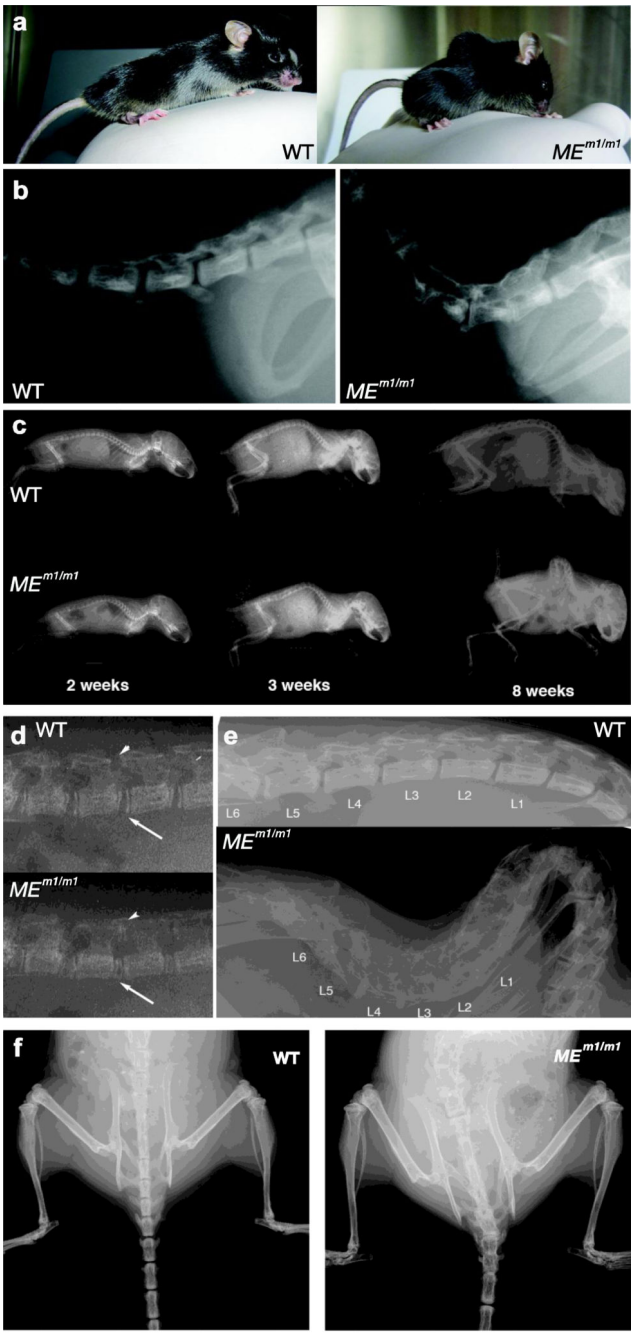

Figure 2. Severe spine degenerative changes associated with kyphoscoliosis in *ME*$^{m1/m1}$ mice

a) Photographs of WT and *ME*$^{m1/m1}$ littermates, showing lordosis and kyphosis in *ME*$^{m1/m1}$; note also dorsiflexed tail in *ME*$^{m1/m1}$. b) Lateral radiographic view of adult WT and *ME*$^{m1/m1}$ littermates, displaying junction between sacral and caudal vertebrae. c) Lateral radiographic views of WT and *ME*$^{m1/m1}$ littermates at 2, 3, and 8 weeks, as indicated. d) Higher magnification at 2-weeks: note narrowing of joint spaces between L4 and L5, arrow (anterior) and arrowhead (posterior). e) Higher magnification of lateral view of lumbar spine at 10 weeks. f) Anterior-posterior (AP) view at 10 weeks. Note in *ME*$^{m1/m1}$ mouse, the

marked scoliosis and the loss of distinct margins (spontaneous fusion) between vertebrae throughout the lumbar, sacral, and caudal regions.

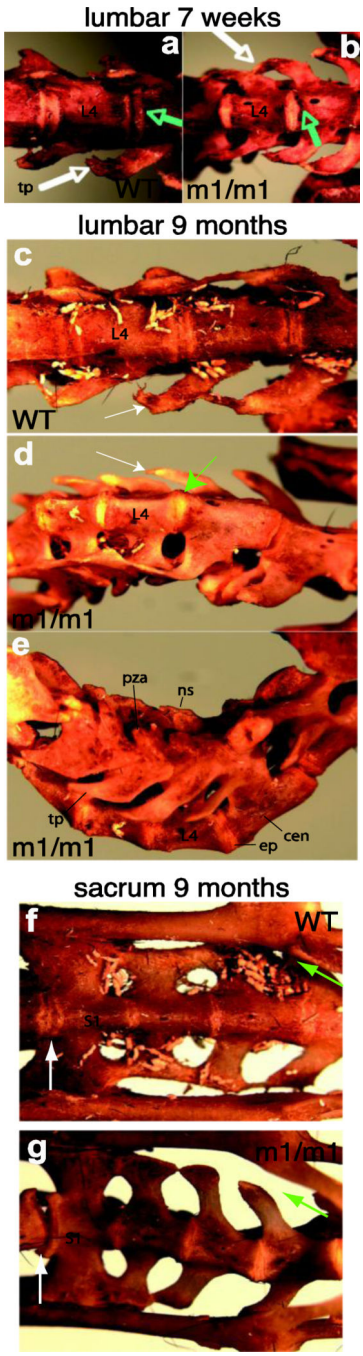

Figure 3. Analysis of cleared specimens

Cleared skeletal specimens obtained from dermestid beetle treatment. In all figures, rostral is to the left. Lumbar (a–e) and sacral regions (f, g) are shown in ventral (a–c, f, g), lateral (e), or oblique (d) views. At 7 weeks, mutants display protruding epiphyses (b, green arrow, compare to a), narrowed intervertebral spaces (b, yellow arrow) and rostrally-elongated transverse processes (b, white arrow, compare to a). Panels c, d, and e depict 9 months lumbar spine, which show similar dysmorphologies as in a and b: (green arrows, protruding epiphysis, white arrows, dysmorphic transverse processes). In panel e, note that the L3-L6

segment is fused in lordosis: centra (cen) are fused with prominent epiphyses (ep); the dorsolateral articulations, comprising the pre- and postzygapophysis (pza) processes are fused to their adjacent counterpart, and neural processes (ns) are short and also fused. Panels f and g: The sacrum of mutants is scoliotic, with an unstable and hypertrophic lumbosacral joint (white arrow, g) and widening of the sacrococcygeal joint (green arrow, g). e, epiphysis; c, centrum; ns, neural spine; pza, prezygapophysis; tp transverse process.

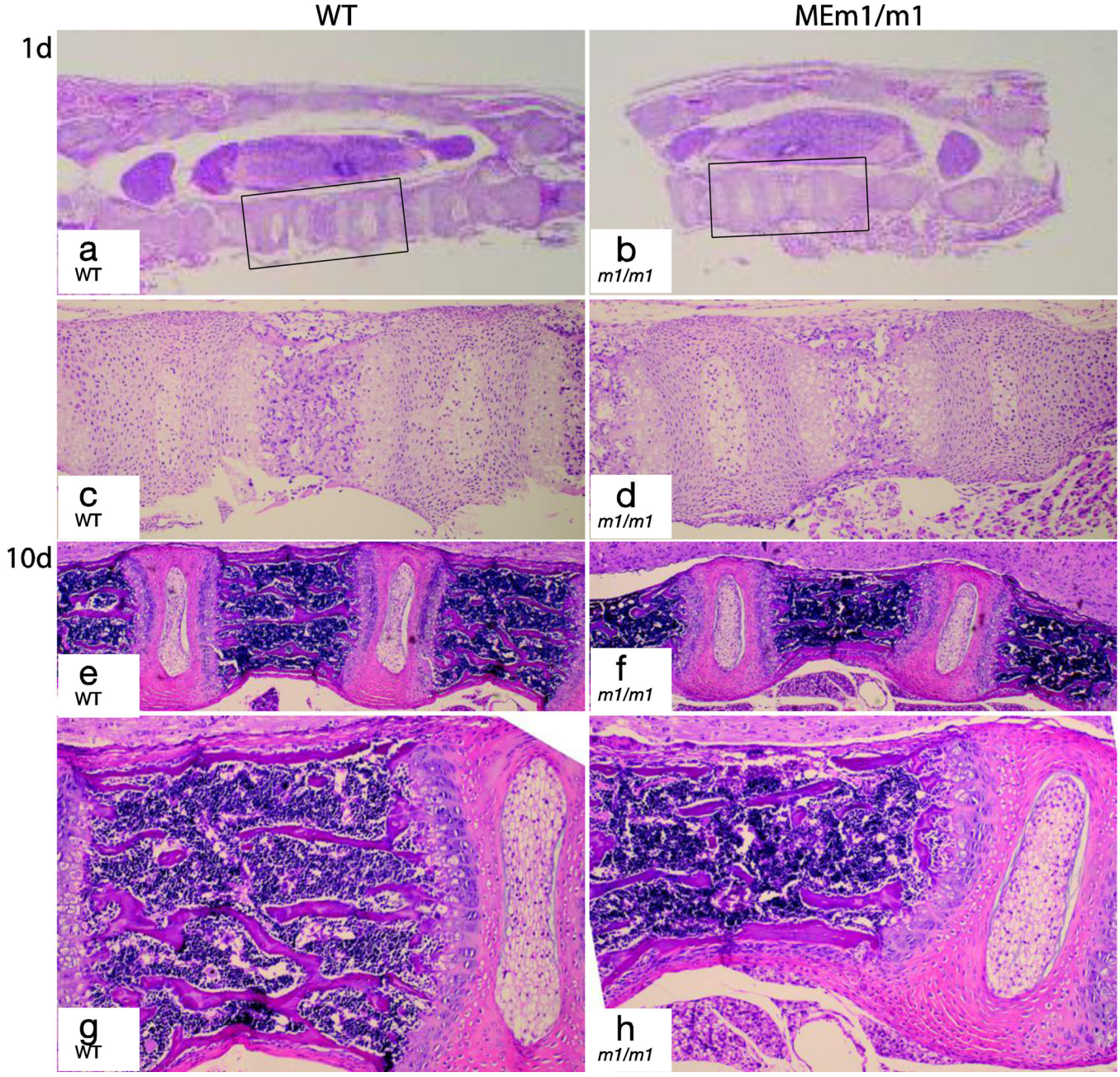

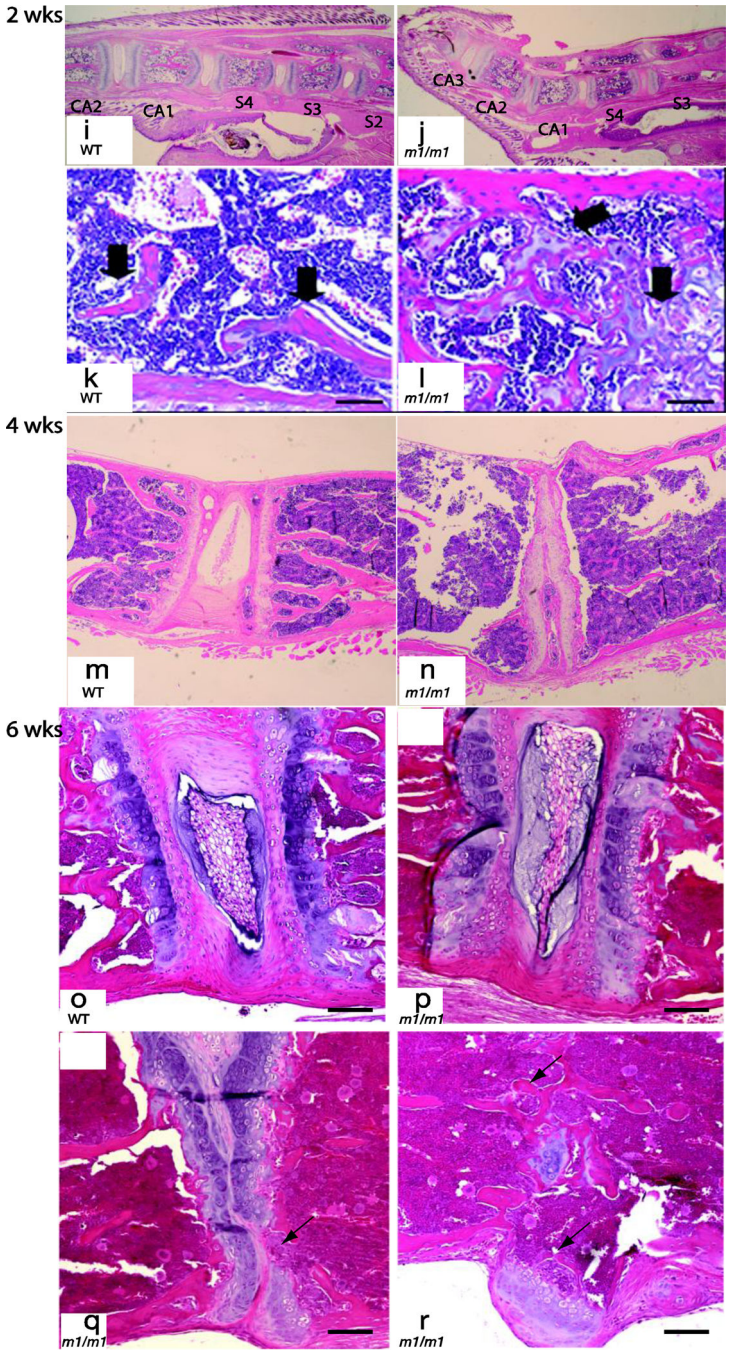

Figure 4. Histologic analysis of spine in *ME*$^{m1/m1}$ mice

Representative H&E-stained sections from one day (a–d), 10 day (e–h), two (i–l), four (m and n), and 6 week-old (o–r) mice show a range of spinal abnormalities in mutants. Panels a–d show sacral region at low and high power, with no demonstrable difference between WT and *ME*$^{m1/m1}$ mice at one day of age. At 10 days (panels e–h), there is evident osteopenia in the lumbar region of *ME*$^{m1/m1}$ mice, though differences are subtle. At 2 weeks, marked delay of endochondral ossification of lumbar vertebral growth plates is present in the mutant (l, black arrow). In the wildtype littermate, cartilage is restricted to physeal plates

(k). At 4 weeks, lumbar discs show partial collapse in $ME^{m1/m1}$ mice (panel n). Panels o–r illustrate various disc changes in the lumbar spine at six weeks. Compared to WT, $ME^{m1/m1}$ mice show a progression from relatively normal disc morphology (p), to narrowed intervertebral space, to disappearance of the nucleus pulposus and loss of cartilage (arrow, q), and fusion of vertebrae (arrows, r). Note also the exostosis in r. Bar = 50 μm.

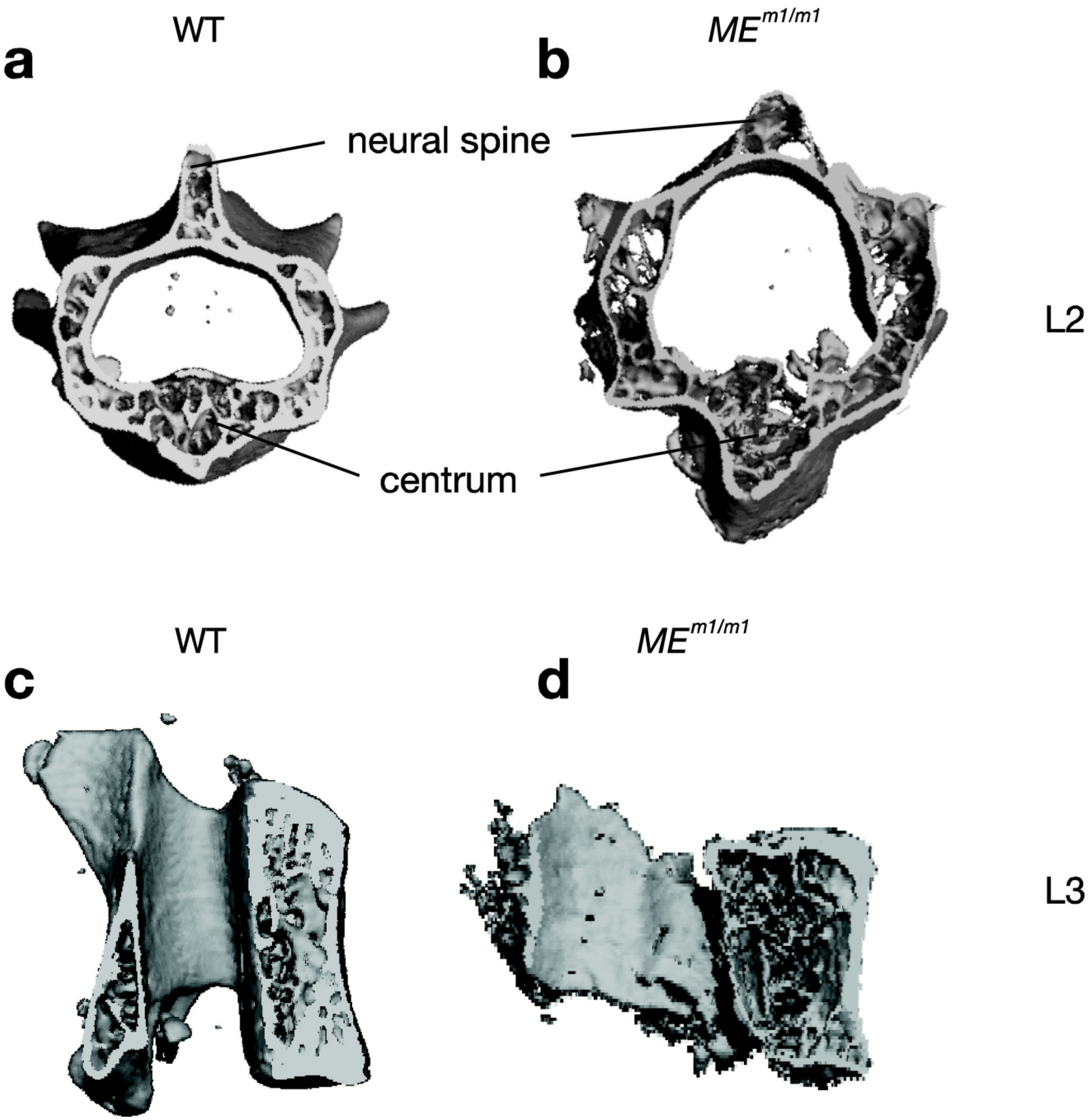

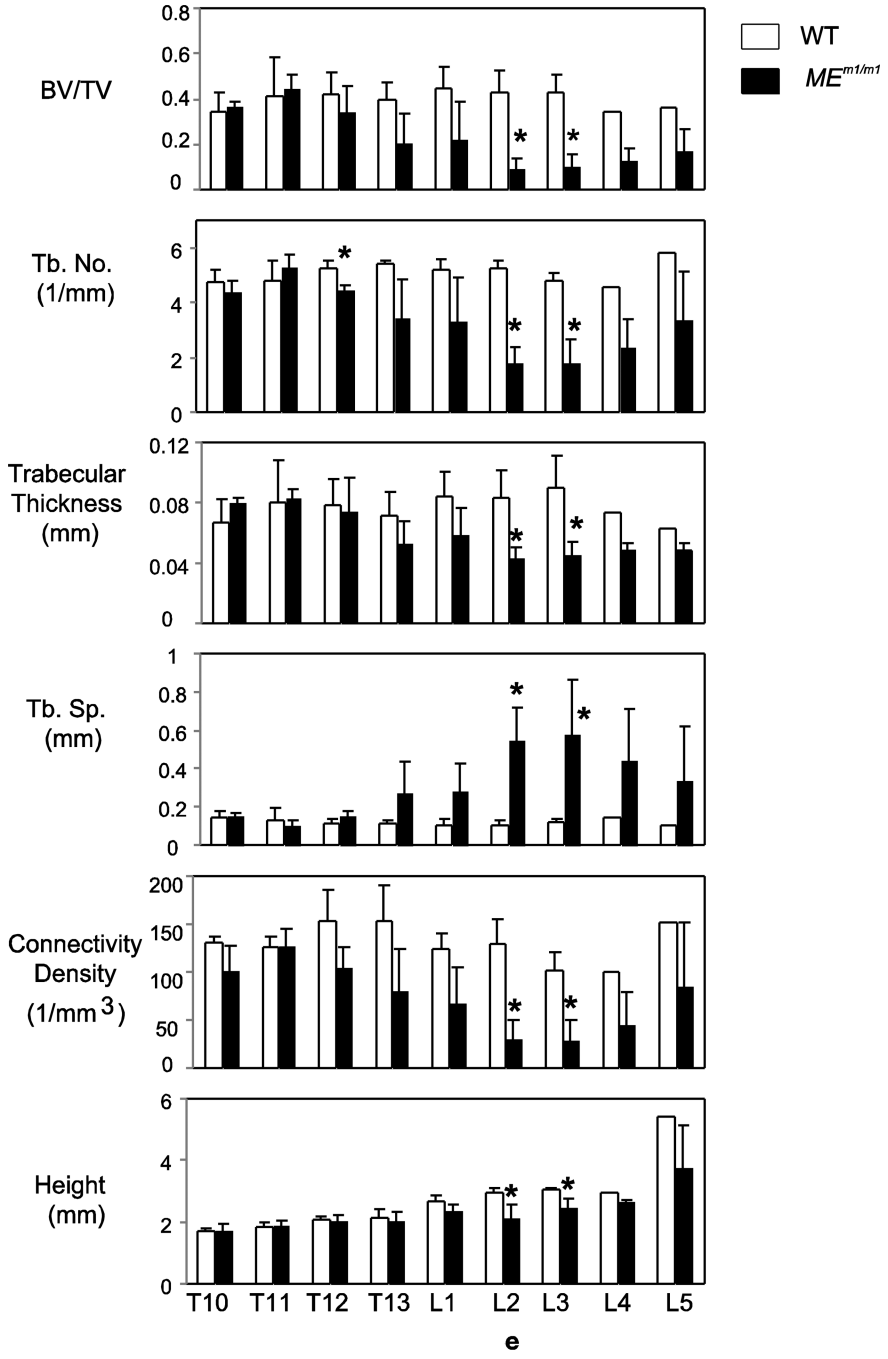

Figure 5. µCT analysis of vertebral bones of MEm1/m1

µCT analysis of vertebral bones of *ME*$^{m1/m1}$.day 1, 6, 10, and 3 month-old mice. a-d. µCT images of L2 and L3 vertebrae from wildtype and mutant mice. **e**. Individual vertebral bodies from T10 to L5 were isolated from 3-month-old animals and were subjected to µCT analysis. Values are the mean ± SD of 3 animals; *p<0.05; BV, bone volume; TV, total volume; Tb.No, trabecular number; Tb.Th, trabecular thickness; Tb.Sp, trabecular spacing; Conn.D, connectivity density.

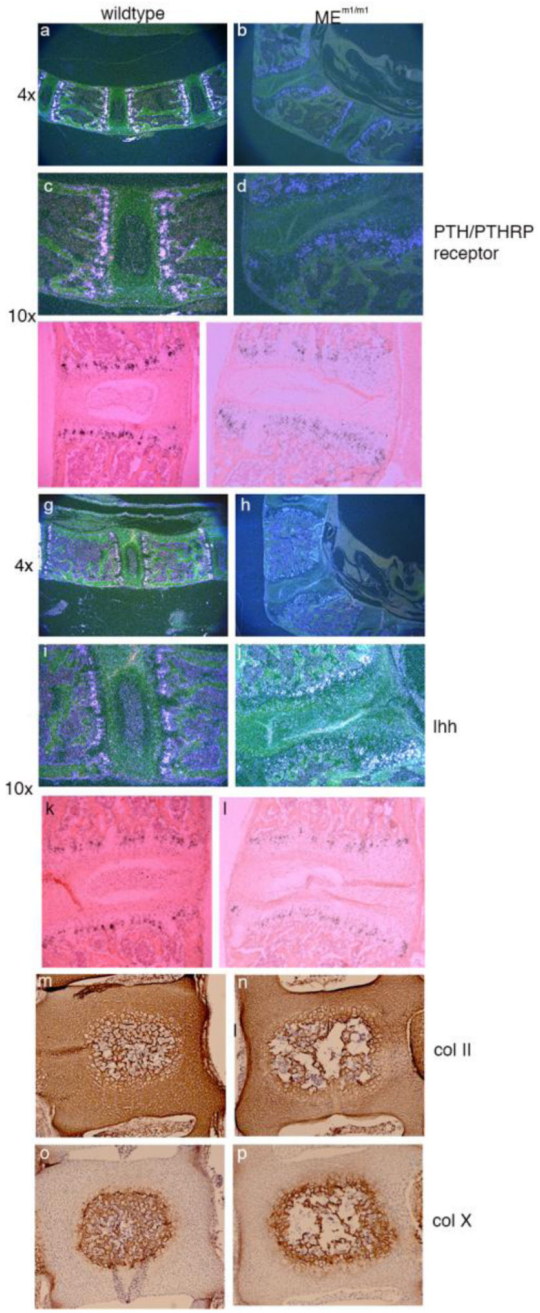

Figure 6. Analysis of endochondral bone formation. Panels a-l

In situ hybridization of adult lumbar spine *for Prp* (PTH/PTHRP receptor) (panels a-f; a-d, dark field; e, f, bright field) and *Ihh* (Panels g-l; g-j, dark field; k, l, bright field). Original magnification is given to the left. **Panels m-p**. Immunohistochemistry for collagen 2a1 and collagen 10a1 in newborn wildtype and *ME*$^{m1/m1}$ mice. Coronal sections of L4 vertebrae in paraffin. Panels m, n: collagen 2a1 stain; Panels o and p: collagen 10a1 stain. Collagen 2 is expressed throughout the early vertebral body and IVD, while collagen 10a1 is limited to the mineralizing core of the vertebral body.

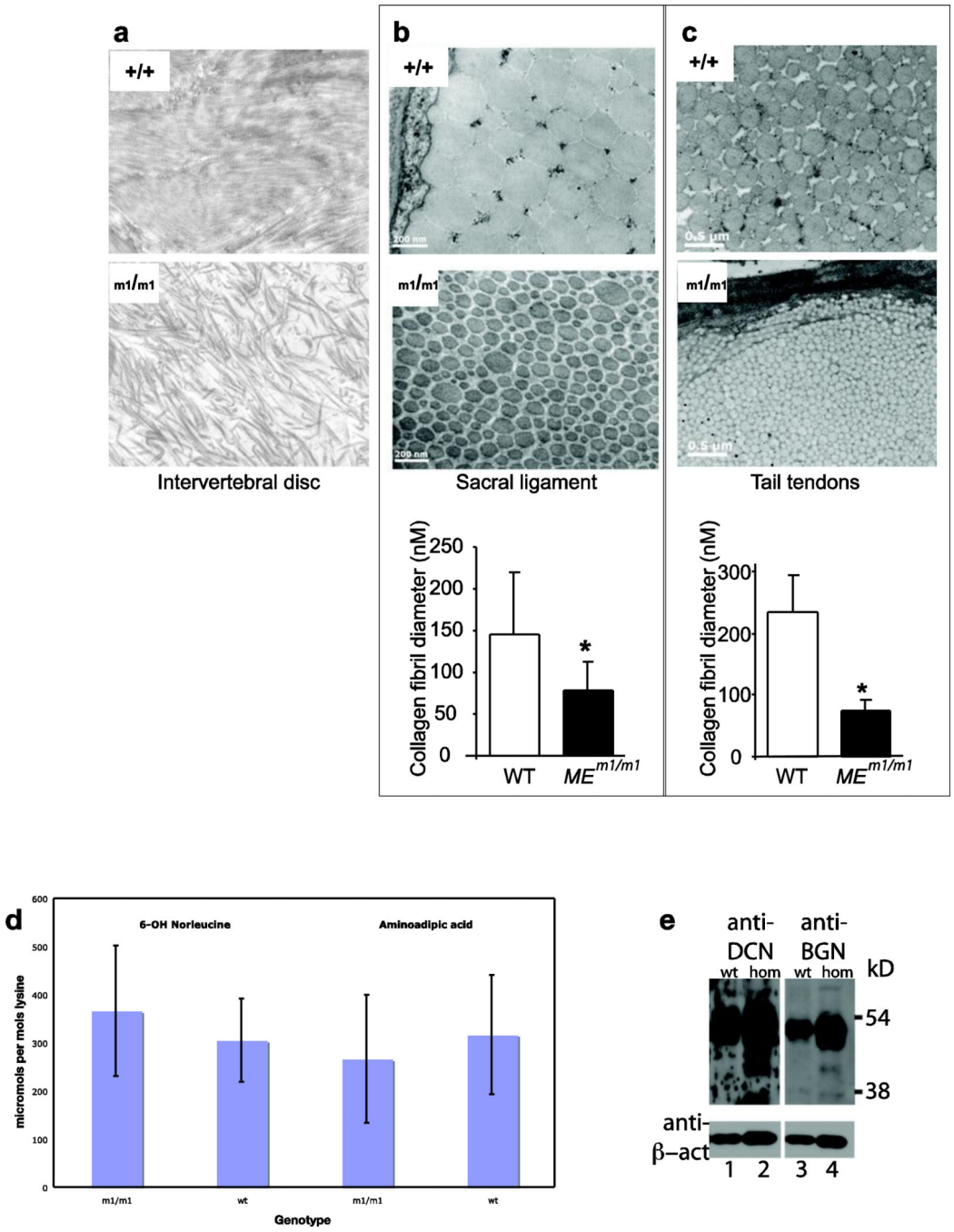

Figure 7. Analysis of collagen

a. Ultrastructural analysis of collagen fibrils in intervertebral disc at one week. b. sacral ligament at 3 months; and c. tail tendon at three months of WT and $ME^{m1/m1}$ mice EMs show reduced diameter but increased number of collagen fibrils in $ME^{m1/m1}$ (b and c). Below are bar graphs showing the mean ± SD of average fibril diameter for genotypes. Three equal areas were scanned. Fibrils were enumerated within the same area. Data are from one pair of 3 month-old mice. *p <0.05. d. Analysis of skin collagen samples for allysine, by conversion to either 6-OH norleucine via reduction or 2-aminoadipic acid via

oxidation. Samples with the genotypes indicated were analyzed. **e**. Western blot analysis of lumbar vertebrae for decorin (lanes 1, 2) and biglycan (lanes 3, 4) as indicated. Bottom panel shows reanalysis of the same blot for β-actin. To the right are molecular weight markers in kilodaltons.

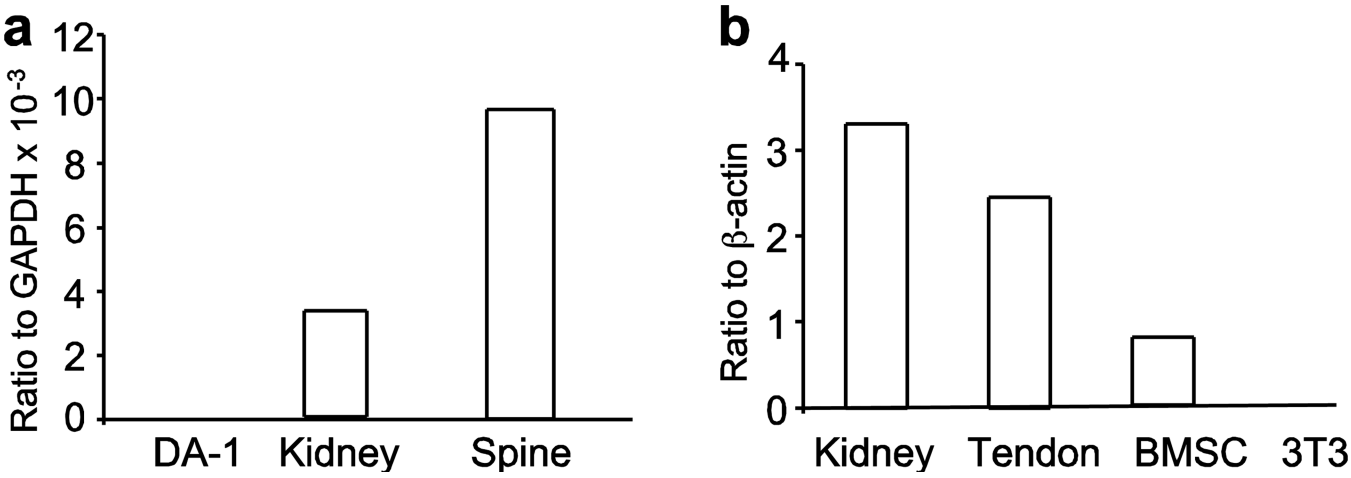

Figure 8. Quantitative reverse transcriptase-PCR analysis of RNA for ME in wildtype mice

Panel a: analysis of ME transcripts in DA-1 leukemic cells, kidney, and in spine. Panel b: analysis of ME transcripts in kidney, primary tenocyte cultures, bone marrow mesenchymal stem cells (BMSC), and NIH 3T3 cells.

Bone. Author manuscript; available in PMC 2015 May 21.

Table 1

a. Biomechanical testing of mutant and wildtype femurs from 3.5 month male mice.

	WT		*ME*$^{m1/m1}$			
	Avg	**SD**	**Avg**	**SD**	**T-test**	**conclusion**
Femoral Length	15.873	0.196	15.603	0.759	0.575	Equivalent
Min Bend Moment of Inertia (mm^4)	0.186	0.032	0.123	0.016	**0.003**	KO are 34% less
Max Bend Moment of Inertia (mm^4)	0.426	0.090	0.232	0.045	**0.002**	KO are 46% less
Polar Moment of inertia (PMOI)(mm^4)	0.611	0.121	0.356	0.062	**0.002**	KO are 42% less
Area (mm^2)	1.036	0.095	0.810	0.086	**0.004**	KO are 22% smaller
Imin/Cmin (mm^3)	0.262	0.031	0.193	0.024	**0.005**	KO are 26% less
Imax/Cmax (mm^3)	0.378	0.051	0.244	0.031	**0.001**	KO are 35% less
Cortical Thickness (mm)	0.215	0.013	0.194	0.016	0.055	KO are 10% thinner
BMD (mgHA/cc)	1126	23	1125	13	0.937	BMD is same
Min Radius (mm)	0.707	0.039	0.636	0.018	**0.004**	KO are 10% thinner
Max Radius (mm)	1.120	0.082	0.943	0.073	**0.007**	KO are 16% thinner
eliptical ratio of Cmax to Cmin	1.585	0.087	1.486	0.130	0.221	are slightly more circular
PMOI * BMD	209	39	138	18	**0.004**	

b. Biomechanical testing of mutant and wildtype femurs from 3.5 month male mice.

	WT		*ME*$^{m1/m1}$			
	Avg	**SD**	**Avg**	**SD**	**T-test**	**Conclusion**
Max Stiffness (N/mm)	153	11	122	20	**0.023**	KO are 20% less stiff overall
Young's Modulus, E (MPa)	8933	1042	10588	720	**0.017**	KO material is 18% is stiffer
Yield Load (N)	16.9	2.2	11.2	0.8	**0.000**	KO able to withstand 34% less load
Yield Deflection (mm)	0.134	0.013	0.113	0.009	**0.016**	Deforms 16% less before yielding
Yield Bending Moment (N*mm)	67.8	8.6	44.8	3.4	**0.000**	KO Able to withstand 34% less moment
Yield Stress (MPa)	129.6	5.9	116.7	10.1	0.052	KO material withstands 10% less pressure
ε_{yield} or Yield Strain (mm/mm)	0.0178	0.0026	0.0130	0.0015	**0.005**	KO material is 27% more brittle
Max Load (N)	21.3	3.8	16.2	2.1	**0.024**	KO 24% less max load
Deflection at Max load (mm)	0.234	0.048	0.229	0.014	0.822	Deflection at is equivalent

b. Biomechanical testing of mutant and wildtype femurs from 3.5 month male mice.

	WT		*ME*$^{m1/m1}$			
	Avg	**SD**	**Avg**	**SD**	**T-test**	**Conclusion**
Post Yield Deformation(mm)	0.100	0.053	0.117	0.020	0.496	Ductility is equivalent
Max Bending Moment (N*mm)	85.4	15.3	64.9	8.2	**0.024**	KO 24% lower Max moment
Max Stress (MPa)	162.5	11.1	167.7	5.7	0.356	Material strength is equivalent
ε_{max} or Max Strain (mm/mm)	0.0311	0.0072	0.0273	0.0016	0.237	Material ductility is equivalent
Ductility (ε_{max} - ε_{yield}) (mm/mm)	0.0133	0.0072	0.0143	0.0028	0.754	Material ductility is equivalent
Energy to Yield (N*mm)	1.28	0.25	0.72	0.03	**0.001**	KO absorb 43% less energy before Yielding
Energy to Max (N*mm)	3.28	1.24	2.40	0.45	0.141	KO absorb 27% less energy to Max (NS)

Abbreviations: Imin, moment of inertia about the minor axis of the cross section; Cmin, perisoteal radius along the minor axis of the cross section; BMD, bone mineral density; Cmax, perisoteal radius along the major axis of the cross section; PMOI, Polar moment of inertia

Abbreviations: N, newtons; MPa, megapascals; KO, knockout (*ME*$^{m1/m1}$); NS, not significant.

Bone. Author manuscript; available in PMC 2015 May 21.